Title

Photoelectron Storage at the WO3/TiO2 Interface: Modeling in Ambient Conditions from First-Principles Calculations

Journal

ACS Catalysis, 13(15)

ISSN

2155-5435

Authors

Li, Yichen
Cheng, Dongfang
Wei, Ziyang
et al.

Publication Date

2023-08-04

DOI

10.1021/acscatal.3c01756

Photo-electron storage at the WO_3/TiO_2 interface: modeling in ambient conditions from first-principle calculations

Yichen Li[†], Dongfang Cheng[‡], Ziyang Wei[‡], Philippe Sautet[†‡]*

[†] Department of Chemistry and Biochemistry, University of California, Los Angeles, California 90095, United States

[‡] Department of Chemical and Biomolecular Engineering, University of California, Los Angeles, California 90095, United states

*** Corresponding Author**

email: sautet@ucla.edu

Abstract

Using first-principle calculations, we showed that monoclinic WO_3(001) preferentially forms a reconstructed monolayer on the anatase TiO_2(001) surface. We thoroughly examined the structure of WO_3/TiO_2 surface under ambient conditions, i.e. in equilibrium with gas-phase O_2/H_2O or H_2/H_2O under a range of pressure and temperature, or in aqueous solution under a range of pH and electrochemical potential. Based on the WO_3/TiO_2 surface structures at different potentials, we proposed the proton-coupled electron transfer (PCET) reaction pathway during charging, and oxygen reduction reaction (ORR) pathways during discharging, which account for its reversible electron storage ability. With electronic structure analysis, we depicted the charge separation effect of WO_3 on TiO_2, and the electron storage effect of WO_3.

Keywords: photocatalysis, titanium dioxide, tungsten trioxide, first principle calculation, electron storage, proton-coupled electron transfer, oxygen reduction reaction

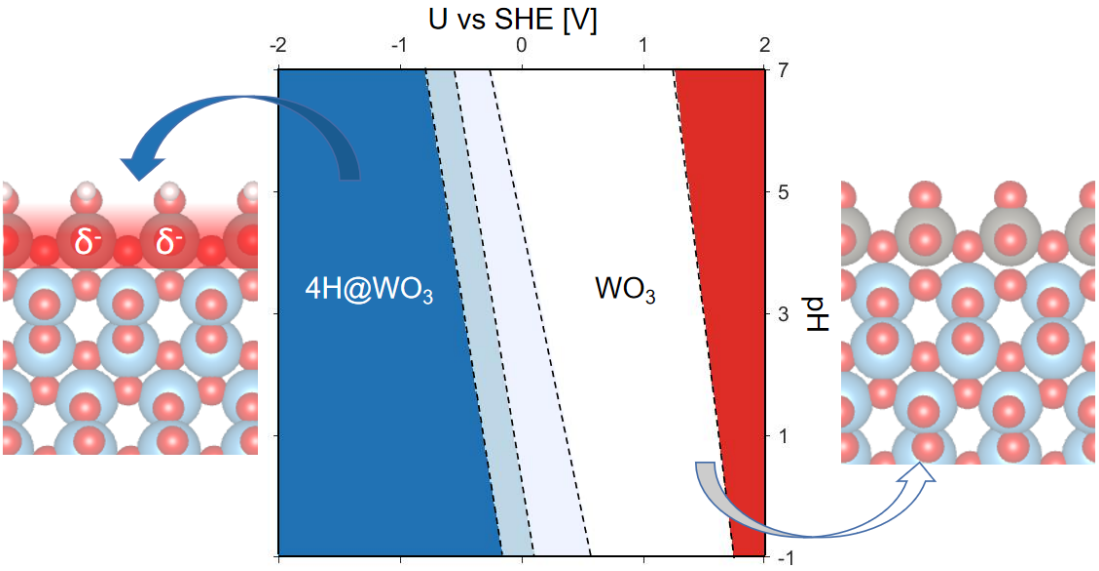

Introduction

Titanium dioxide (TiO_2) is the most widely used catalyst in heterogeneous photocatalysis, though suffering from high charge carrier recombination rate (lifetime ~10^{-12} s) and large band gap (~3.2 eV) requiring photons in the UV region [1-2]. To improve the performance, TiO_2 is often hybridized with cocatalysts with narrower band gap [3]. For example, WO_3 is often chosen as a cocatalyst for TiO_2, for its 2.7 eV band gap and excellent stability. This hybridization assists electron-hole separation and mitigates electron-hole recombination. WO_3 on TiO_2 has already been exploited for the degradation of pollutants and antibiotics [4-8].

The WO_3 co-catalyst is able to store the electrons provided from photo-generated electron-hole pairs on TiO_2. While the holes participate in oxidation reactions on the TiO_2 substrate, the electrons can be stored in WO_3, with the formation of a bronze compound M_xWO_3 (M = H, Li, Na, $x \leq 1$), and restored when needed to be used in a discharging reaction. This charging-discharging cycle is associated with the electrochromism/photochromism properties of WO_3 [9]. For example, for M=H:

$$WO_3 + (xe^- + xH^+) \rightarrow H_xWO_3 \quad \text{(charging)}$$

$$H_xWO_3 \rightarrow WO_3 + (xe^- + xH^+) \quad \text{(discharging)}$$

Protons from the solution or ambient water serve as charge compensation. This capability of WO_3 opens up the opportunity of storing photo-generated electrons during daytime, and releasing the stored energy for reactions later, even in dark conditions. This idea was proven practical in anticorrosion [9] and organic pollutant oxidation [1, 10-12].

Aside from photocatalysis, V_2O_5-WO_3/TiO_2 is also an extensively used commercial catalyst in thermocatalysis for selective catalytic reaction (SCR) of NO_x [13-14], for its high stability and selectivity [15]. This can efficiently reduce NO_x emission produced by the combustion of fossil fuels.

In 1992, Tennakone *et al.* first found that WO_3/TiO_2 may turn blue under light radiation, and quickly bleach when exposed to oxygen. They credit this electrochromism to WO_3 surface hydroxylation [16]. In 2001, Tatsuma *et al.* first adopted this energy storage ability of WO_3/TiO_2 in anticorrosion [9], and credit the energy storage ability to hydrogen intercalation into WO_3 bulk lattice [10]. In 2009, Sajjad *et al.* performed thorough studies on WO_3/TiO_2 photocatalytic reactivity, proposing that sol-gel fabricated samples with WO_3 monolayer in epitaxy on TiO_2 are more reactive than calcined ones with a more WO_3 bulk structure [17]. Also in 2009, Zhao *et al.* successfully used WO_3/TiO_2 to store photo-electrons for heavy metal ion reduction in the dark. They also verified the electron storage in W with electron spin resonance (ESR) measurement [18]. In 2018, Khan *et al.* did another thorough study more focused on WO_3/TiO_2 charge storage ability, agreeing that the monolayer WO_3 coverage is optimal [19]. In 2019, Zhou *et al.* decorated a-TiO_2(001) with WO_3 and found enhanced water decontamination efficiency [20]. Computational studies about WO_3/TiO_2 photochemistry are relatively scarce, though in 2013, Negreira *et al*. first proposed a V_2O_5-WO_3 monolayer model on TiO_2(001) for NO_x selective catalytic reaction [21]. To fill the gap, we first aim at a fundamental understanding from first principle calculations of the surface structure of the WO_3/TiO_2 catalyst under ambient conditions. We have selected various conditions; i.e. in equilibrium with gas-phase O_2/H_2O or H_2/H_2O, or in aqueous-phase solution. In the latter case, based on the surface structures of WO_3/TiO_2 at different potentials, we show that proton adsorption/desorption processes accompany the reversible electronic charge storage, to satisfy charge balance. With electronic structure analysis, we depict the charge separation effect of WO_3 on TiO_2, and confirm that the photo-electron is stored in W 5d states.

Methods

Density functional theory (DFT) calculations are performed using the Vienna ab initio simulation package (VASP) [22-24]. The exchange-correlation energy is calculated using the Perdew-Burke-Ernzerhof (PBE) functional [25]. The projector-augmented wave method is used to describe the core electrons [26]. The one-electron wave functions are developed on a basis set of plane waves with an energy cutoff of 400 eV. The dDsC dispersion correction method is used to account for van der Waals forces [27-28]. Energy differences between steps in SCF cycles are converged to 10^{-6} eV. Atomic positions are relaxed until the forces are less than 0.05 eV/Å^{-1}. To correct for the self-interaction error of Ti 3d electrons, a Hubbard-like repulsion term is added using Dudarev's approach (PBE+U) [29], with $U_{Ti} = U-J = 3.5$ eV, determined using linear response [30]. For better accuracy in the electronic structure analysis and for the charge carrier localization, single-point calculations were performed with the Heyd-Scuseria-Ernzerhof functional (HSE06) [31]

using the PBE+U_{Ti} geometry. Photo-generated electrons (holes) are simulated by adding (removing) electrons in the supercell. The surface charging method with the implicit solvation model and the linearized Poisson Boltzmann approach is used to simulate the solvent and electrolyte, when the catalyst is considered to be in an aqueous solution.

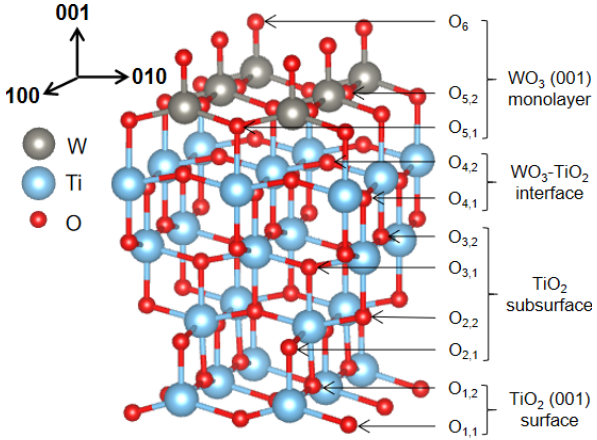

Figure 1. **Structure of the supported m-WO_3(001) monolayer on a-TiO_2(001).** The a-TiO_2(001) surface is modeled by 4 O-Ti-O trilayers, with a m-WO_3(001) monolayer epitaxed on top.

The monoclinic crystal system is the most stable phase of WO_3 below 600 K, while anatase is also a common and stable phase of TiO_2. Many studies found that the highest electron storage ability [18-19, 32]and photocatalytic reactivity [17] of WO_3/TiO_2 occurs a WO_3 loading corresponding to ~4 % W/T atom ratio, and drops at higher loadings. Considering the surface area of the TiO_2 support (47 m^2/g), this 4% W/T atom ratio is equivalent to a monolayer coverage. At optimal loading, X-ray diffraction spectra in many studies do not show any characteristic peak of WO_3, indicating the absence of 3D WO_3 crystals[17, 33]. High-resolution transmission electron microscopy confirms the absence of WO_3 clusters or nanoparticles [17-18]. All these experiments indicate that WO_3 tends to form an ultrathin layer on TiO_2 at optimal loading. At higher loadings, WO_3 agglomerates into particles.

We choose anatase TiO_2(001) as substrate, because TiO_2(001) usually has very high reactivity and plays a crucial role in anatase nanoparticle reactivity and photocatalytic activity [34-35]. The existence of TiO_2(001) in WO_3/TiO_2 has been verified by XRD in WO_3/TiO_2 experiments [17-19, 32]. In addition, Raman experiments showed that the percentage of TiO_2(001) facet initially increases upon WO_3 loading, from 6 % on pure TiO_2 to 21.5 % at optimal WO_3 loading. Moreover, a further increase of WO_3 loading results in a simultaneous decrease of the TiO_2(001) percentage and electron storage capacity [19]. Hence, TiO_2(001) plays a major role, in the presence of the WO_3 layer, for electron storage, justifying our choice. m-WO_3(001) has lattice constants, for the p(2×2) supercell, of 2a = 2b = 7.58 Å, while a-TiO_2(001) has lattice constants of a=7.31 Å, b=7.55 Å, and this small lattice mismatch could lead to stronger adhesion between m-WO_3(001) and a-TiO_2(001), with minimal strain in the b direction (Supporting Note 1). Thus, the model formed by m-WO_3(001) layers on a-TiO_2(001) substrate is chosen in this study. In the case of the m-WO_3(001) monolayer model (Figure 1), a p(2×2) 4-layer a-TiO_2(001) slab stands for the substrate, and a p(2×2) m-WO_3(001) monolayer adheres on this substrate [21]. All layers are relaxed, so that the top surface models the supported WO_3 monolayer, while the bottom surface models TiO_2 areas that are not covered by WO_3. The Brillouin zone is sampled using a 3×3×1 k-mesh [36], and detailed tests show that this k-mesh provides converged energies (Supporting Note 9).

Results and discussion

Adhesion structure and number of layers of WO_3 on TiO_2

The most stable calculated structure for a m-WO_3(001) monolayer on a-TiO_2(001) is shown in Figure 1, and it shows an adhesion surface energy of -1.40 J/m^2. The definition of adhesion surface energy, and other tested adhesion structures of m-WO_3(001) monolayer on a-TiO_2(001) are listed in Supporting Note 2. Unlike a non-supported m-WO_3(001) surface, which shows 1/2 ML terminal oxygen coverage on surface W atoms (Supporting Figure S2a); the supported WO_3 monolayer has 1 ML terminal oxygen coverage. Each W atom is in a highly distorted octahedral environment, with one O atom of the TiO_2 surface layer included in the distorted octahedron. The strongest bond between the WO_3 monolayer and the TiO_2 surface is between a topmost Ti atom and a O atom from the WO_3 layer. Detailed bond distances for this structure are listed in Supporting Table S1. Notably, the WO_3 monolayer is stretched by 3.6% and 0.4% along [100] and [010] direction due to the small lattice mismatch with TiO_2. Additional WO_3 layers can be constructed on top of the WO_3 monolayer, extending the distorted octahedral arrangement, as shown in Supporting Figure S4. However, the additional layers are only bound to the previous one by weak interlayer W-O bonds (distance 2.46 Å). The adhesion surface energies of the second and third WO_3 layer are -0.35 and -0.52 J/m^2, significantly smaller than adhesion energy of the first WO_3 layer with TiO_2. This indicates that WO_3(001) favors a monolayer epitaxy rather than stacking into multilayers when deposited on TiO_2(001). The findings are supported by numerous experiments. Raman spectra demonstrate that only 2D WO_3 species are present on TiO_2 at low loading, and 3D WO_3 species are not observed until the loading is increased to 8 wt% [37-38]. Additionally, X-ray diffraction analysis indicates the absence of any WO_3 characteristic peak at 0-6 wt%, indicating monolayer coverage at low WO_3 loading [17]. Further catalytic reactivity measurements reveal that the monolayer coverage of WO_3 on TiO_2 (3-10 wt%) exhibits the highest reactivity towards organic pollutant photocatalytic degradation [4]. This also underlines the necessity to study the synergistic effect between the m-WO_3(001) monolayer and the a-TiO_2(001) substrate, rather than take the properties of m-WO_3 bulk or non-supported m-WO_3(001) surface to explain the reactivity of WO_3/TiO_2. Furthermore, we observe a thickness dependent electronic polarity in WO_3 multilayers on TiO_2. At monolayer thickness, the WO_3 layer is spin-neutral; but at bilayers thickness or above, electrons transfer from the topmost WO_3 layer O atoms to the interfacial WO_3 layer W atoms, resulting in uncompensated polarity in WO_3 multilayers. This phenomenon for WO_3 bilayers on TiO_2 can be reflected by both the spin-density distribution and the density of state (DOS) in Supporting Figure S7. Electrons transfer from O p states in the topmost WO_3 layer to W d states in the interface WO_3 layer. This causes the unpaired electrons to show spin density in corresponding orbitals. WO_3 trilayers on TiO_2 also show similar properties. Such layer-dependent polarity has also been reported in other supported ultrathin metal oxide (MgO, ZnO) films [39].

WO_3/TiO_2 stability diagram in experimental conditions

The structure of the WO_3 monolayer in Figure 1 is a simple stoichiometric model, and it does not take into account the influence of the reactants in the environment. Indeed, the surface structure of monolayer WO_3/TiO_2 will vary depending on experimental conditions. In gas-phase photodecomposition reactors [4-5], the WO_3/TiO_2 is in equilibrium with H_2O and O_2 pressure at 298

K. In gas-phase NO_x selective catalytic reduction reactors, the WO_3/TiO_2 is in equilibrium with H_2O and H_2 at elevated temperatures around 400-600 K [40]. To determine the surface structure of WO_3/TiO_2 at realistic experimental conditions, the surface stability for various adsorbates such as O, O_2, H, OH, H_2O, and O vacancy formation, must be compared. For adsorbates with high likelihood to populate the surface at experimental conditions, such as H and H_2O, coverage effect is also included. Details about adsorption energy calculations are discussed in Supporting Note 3,4,5,6 and 7. The results are summarized into the stability diagrams shown in Figure 2, and the corresponding structures are listed in Figure 3.

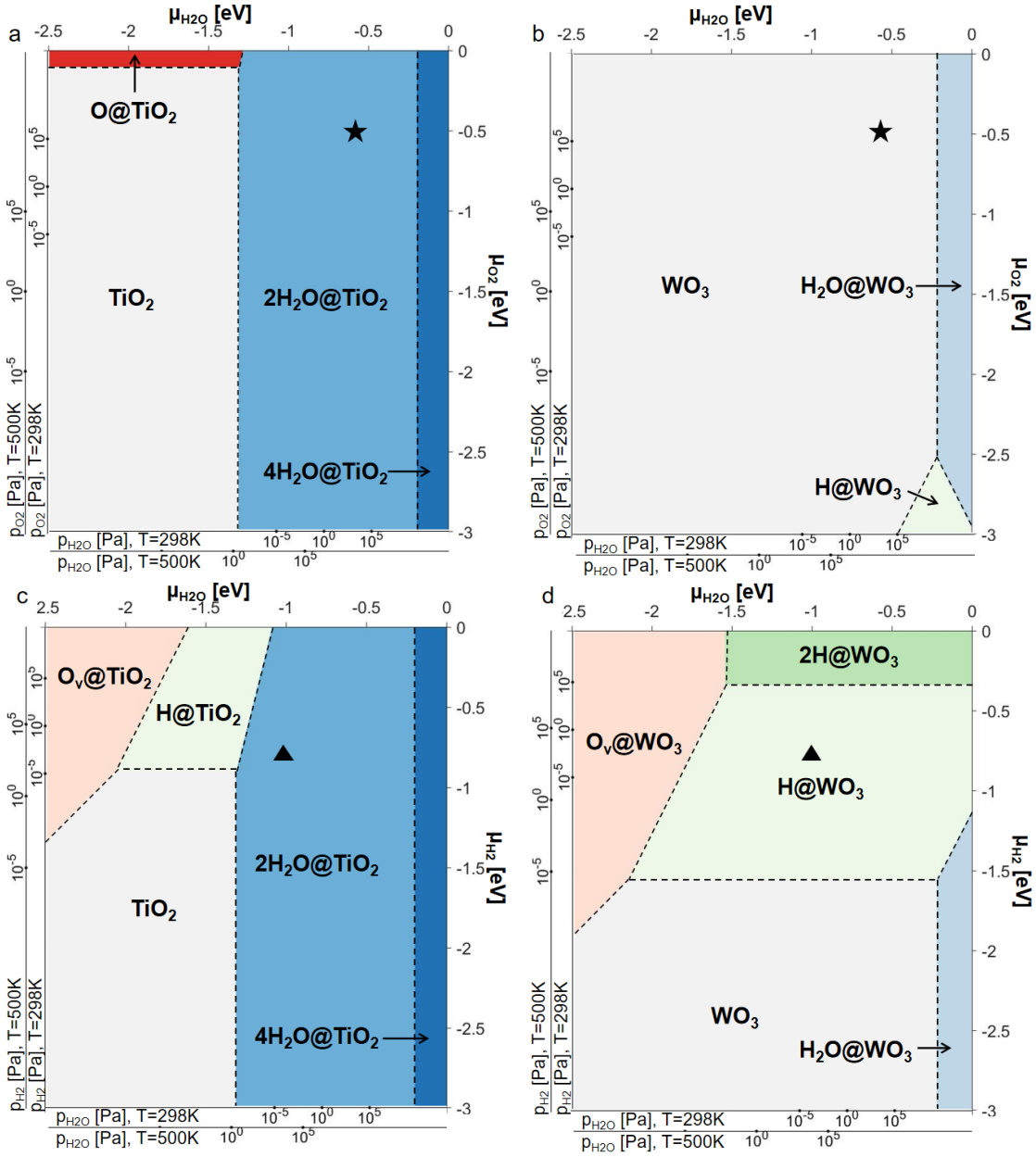

Figure 2. Stability diagrams for the a-TiO_2(001) surface and the supported m-WO_3(001) monolayer on a-TiO_2(001). a) a-TiO_2(001) surface in equilibrium with O_2/H_2O, with O_2/H_2O chemical potentials being used as descriptors (a scale of O_2/H_2O pressure is provided at T = 298 and 500 K). b) Supported WO_3 monolayer on a-TiO_2(001) in equilibrium with O_2/H_2O. c) a-TiO_2(001) surface in equilibrium with H_2/H_2O. d) Supported WO_3 monolayer on a-TiO_2(001) in equilibrium with H_2/H_2O. Corresponding structures are listed in Figure 3. The black stars

correspond to gas-phase reactors at room temperature (p_{O2} = 21 kPa, p_{H2O} = 3.5 kPa [41], T = 298 K) [4-5], usually used for photocatalytic reactions; the black triangles correspond to gas-phase reactors at elevated temperature (p_{H2} = ~1 kPa, p_{H2O} = ~5 kPa, T = 500 K) [40], usually used for NO_x selective catalytic reduction reactions. All amounts of adsorbates correspond to a p(2×2) supercell for the a-TiO_2(001) surface or support.

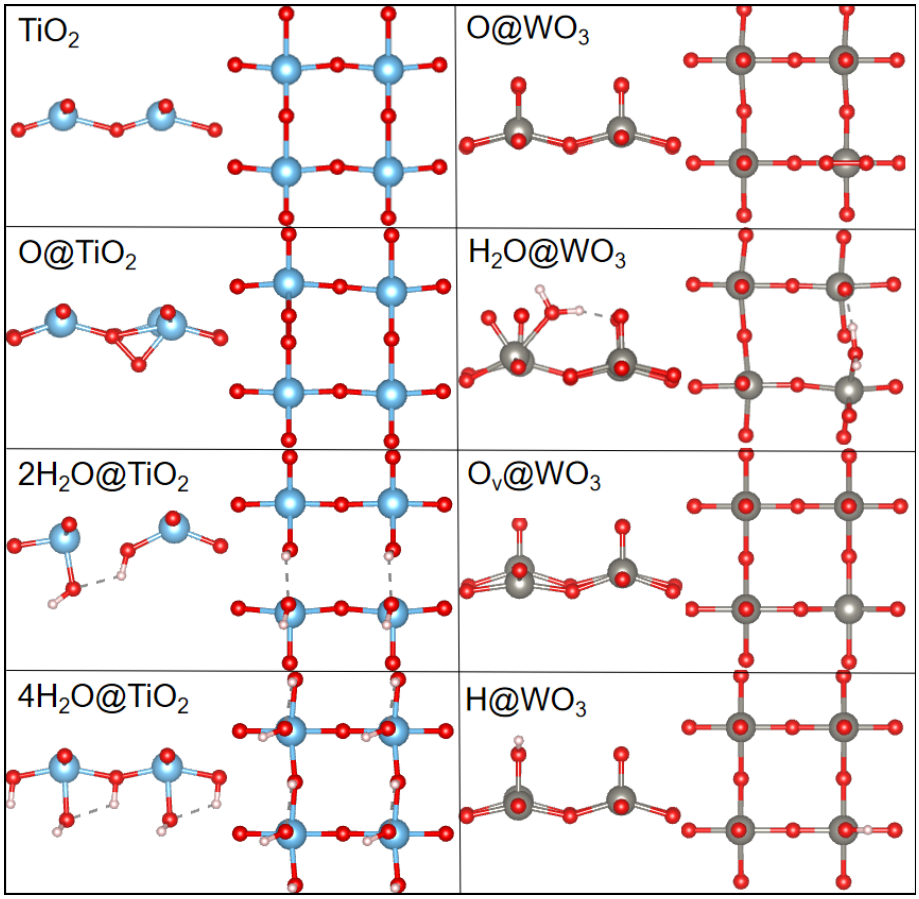

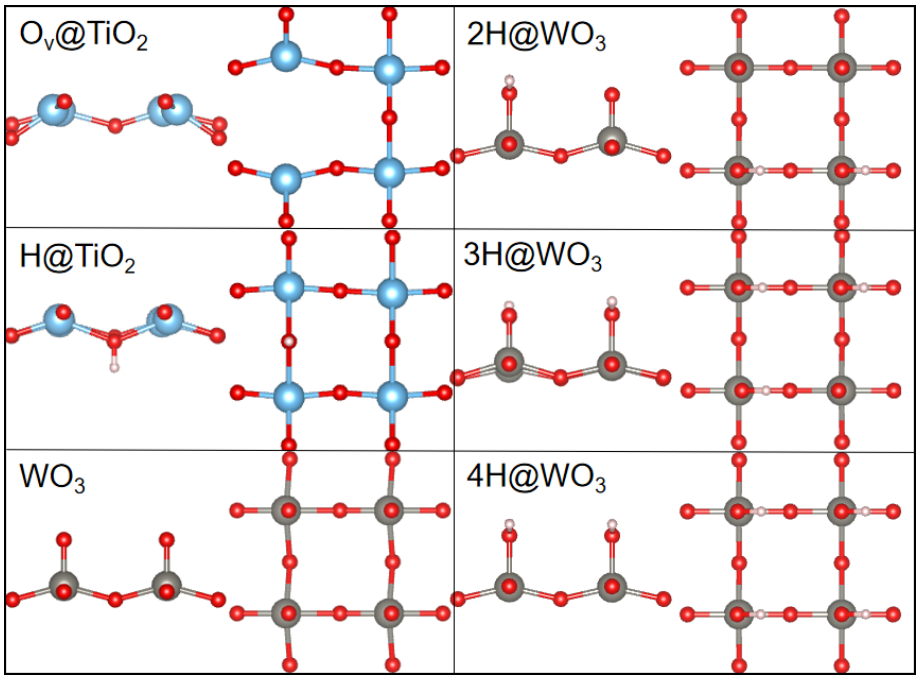

Figure 3. a-TiO_2(001) and supported WO_3 monolayer on the a-TiO_2(001) surface structures with adsorbates, mentioned in the stability diagrams (Figure 2) and Pourbaix diagram (Figure 4). Only the surface layer interacting with the environment is shown. In each panel, the left figure shows the side view and the right figure shows the bottom view (TiO_2 surface) or top view (WO_3 surface). All structures correspond to a p(2×2) supercell for the a-TiO_2(001) surface or support.

According to Figure 2a, when in equilibrium with H_2O and O_2, a-TiO_2(001) is hydrated into $2H_2O$@TiO_2 (1/2 ML of H_2O, 3.43 H_2O/nm^2) at experimental conditions for photocatalytic reactions (p_{O2} = 21 kPa, p_{H2O} = 3.5 kPa [41], T = 298 K) [4-5]. The two adsorbed water molecules dissociate into OH and H and disrupt the bonds of bridging oxygens, leading to the reconstruction and stabilization of the a-TiO_2(001) surface. This surface hydration was already proposed by previous studies, though the optimal coverage is under debate [2]. At water-rich conditions, a-TiO_2(001) could be further hydrated into $4H_2O$@TiO_2 (1 ML of H_2O, 6.85 H_2O/nm^2); while at water-poor conditions, H_2O chemisorption does not occur and a-TiO_2(001) remains bare. At water-poor but oxygen-rich conditions, a-TiO_2(001) could be oxidized into O@TiO_2, although exceedingly high O_2 pressure is needed. According to Figure 2b, the supported m-WO_3(001) monolayer is bare at photocatalysis experimental condition. At water-rich conditions, water molecules could be adsorbed on tungsten atoms (H_2O@WO_3). At water-rich but oxygen-poor conditions, terminal oxygen of the WO_3 monolayer could be hydrogenated, forming terminal hydroxyl (H@WO_3).

According to Figure 2c, when in equilibrium with H_2O and H_2, a-TiO_2(001) is also hydrated into $2H_2O$@TiO_2 at experimental conditions for NO_x selective catalytic reduction reactions (p_{H2} = ~1 kPa, p_{H2O} = ~5 kPa, T = 500 K) [40]. The phase shift among bare TiO_2, $2H_2O$@TiO_2 and $4H_2O$@TiO_2 can also be achieved by manipulating water chemical potential. However, at water-poor but hydrogen-rich conditions, the bridging oxygen of TiO_2 could be hydrogenated and forms hydroxyl (H@TiO_2); at even water-poorer condition, this oxygen could be desorbed and form an oxygen vacancy (O_v@TiO_2). According to Figure 2d, the supported m-WO_3(001) monolayer is hydrogenated into H@WO_3 (1/4 ML, 1.71 H/nm^2) at experimental conditions. The phase shift among bare WO_3, H@WO_3 and 2H@WO_3 can be achieved by manipulating hydrogen chemical potential. At water-rich but hydrogen-poor conditions, water could be adsorbed (H_2O@WO_3). At water-poor but hydrogen-rich conditions, the terminal oxygen of the WO_3 monolayer could be desorbed and form an oxygen vacancy (O_v@WO_3).

Photoelectrochemical cell conditions: WO_3/TiO_2 Pourbaix diagram

In photoelectrochemical cells [19, 32], WO_3/TiO_2 is in equilibrium with aqueous solvent at certain electrochemical potential and pH. Since the prominent role of the WO_3/TiO_2 is its charge storage ability, but pure TiO_2 surface itself has no charge storage ability [32], the pure TiO_2 surface at the bottom of the model is ignored, only the surface structures of the supported WO_3 monolayer are considered. Details about this part of calculations are discussed in Supporting Note 8. The results are summarized into the Pourbaix diagrams shown in Figure 4, with corresponding structures listed in Figure 3.

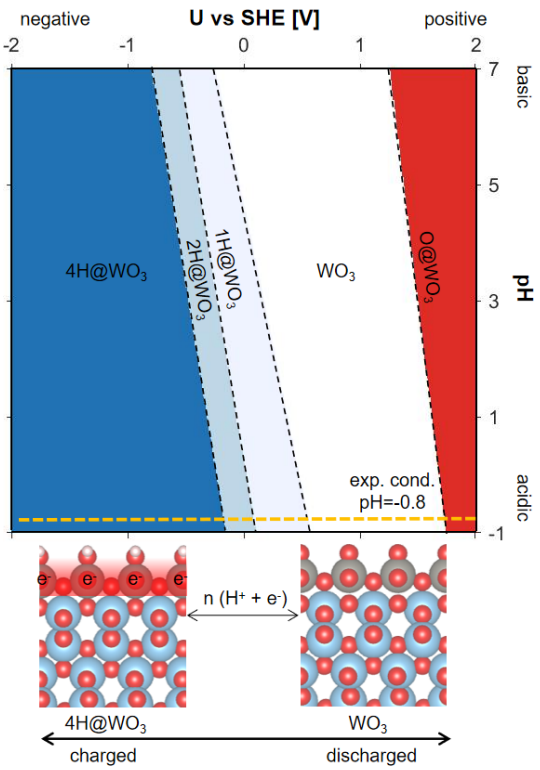

Figure 4. **Pourbaix diagram of supported m-WO_3(001) monolayer on a-TiO_2(001)**, as a function of electrochemical potential U (versus Standard Hydrogen Electrode) and pH. The orange dotted line corresponds to an example experimental condition (pH = -0.8) [32], used for reversible electron storage. All amounts of adsorbates correspond to a p(2×2) supercell.

According to Figure 4, at experimental conditions (pH = -0.8) [32], before light radiation, the supported WO_3 monolayer is not charged and is bare. With light radiation, photo-generated electrons in the TiO_2 conduction band provide a negative potential (-0.7 V vs SHE, corresponding to the conduction band minimum of TiO_2) [2], the bare WO_3 monolayer gradually captures protons and electrons, and finally transits into 4H@WO_3 (all amounts of adsorbates correspond to a p(2×2) supercell). When light radiation is removed, TiO_2 stops generating photo-electrons, 4H@WO_3 gradually releases protons and electrons, and finally relaxes back into bare WO_3. An illustration of the proton-electron desorption process is shown in the reaction pathways of Figure 5b, this process can be achieved via either reactions [19]: (i) 4H@WO_3 reacts with O_2, involving one stored electron and forms 3H@WO_3+$HO_2^{\bullet}$. (ii) 4H@WO_3 reacts with O_2, involving two stored electrons and forms 2H@WO_3+H_2O_2.

$$(*H^+ + e^-) + O_2 \rightarrow HO_2^{\bullet} \quad \text{(i)}$$

$$(2*H^+ + 2e^-) + O_2 \rightarrow H_2O_2 \quad \text{(ii)}$$

The proton-coupled electron transfer on supported WO_3 monolayer is shown in Figure 5a. According to Figure 4, the transition between 0H@WO_3 and 1H@WO_3 happens at U=+0.76 V vs SHE. Here, a solvated proton with explicit water molecules is modeled by the $H^+(H_2O)_4$ cluster. The water cluster configuration was found to help circumvent the unphysical invasion of the implicit solvent into the solvation shell [42]. First, $H^+(H_2O)_4$ approaches the Helmholtz plane near the surface (ΔE=-0.62 eV). Then, the proton binds with the terminal oxygen of WO_3 (ΔE=+0.37

eV, E_a=+0.44eV). Finally, $(H_2O)_4$ returns from the Helmholtz plane to bulk liquid (ΔE=+0.25 eV).

The oxygen reduction reactions utilizing stored proton-electron pair(s) on the supported WO_3 monolayer is shown in Figure 5b. First, O_2 approaches the Helmholtz plane near the surface, and a partial electron transfer occurs from W to O_2 (ΔE=-0.49 eV). Then, $O_2^{\delta-}$ binds with $*H^+$, along with an electron stored in W, and forms $*HO_2^{\bullet}$ (ΔE=-0.82 eV). There are two possible pathways for the following reactions: (i) $*HO_2^{\bullet}$ may directly desorb from the WO_3 monolayer, and forms $HO_2^{\bullet\delta-}$ (ΔE=+0.16 eV), then $HO_2^{\bullet\delta-}$ donate the partial electron back to WO_3 when it leaves the Helmholtz plane (ΔE=+0.42 eV); (ii) $*HO_2^{\bullet}$ may further react with another stored proton-electron pair ($*H^+ + e^-$) and form $*H_2O_2$ (ΔE=-1.71 eV), then H_2O_2 desorb from WO_3 monolayer (ΔE=+0.34 eV). Though $*HO_2^{\bullet}$ and $*H_2O_2$ desorption are endothermic, such processes will be favored from entropic considerations. However, these proton-electron desorption processes are relatively slow, which accounts for the fact that WO_3/TiO_2 is still reactive minutes after the light radiation is removed [32].

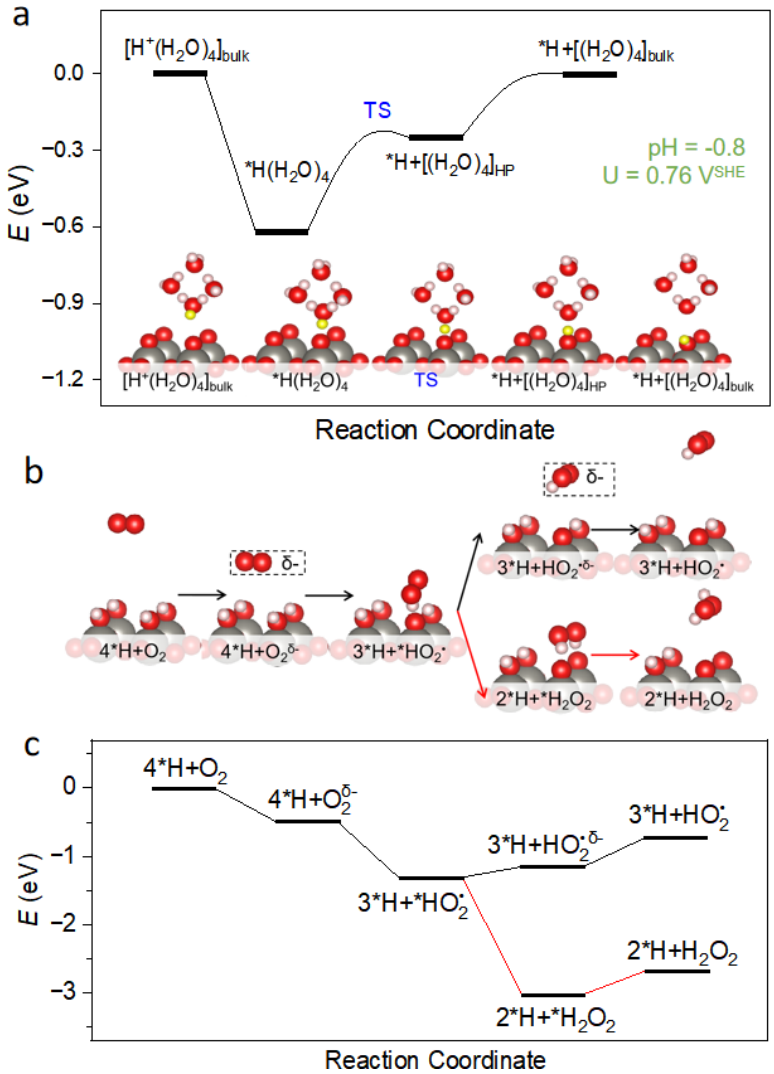

Figure 5. Potential energy diagram of proton-coupled electron transfer and oxygen reduction reactions on the supported m-WO_3 monolayer. (a) Proton-coupled electron transfer. Bare WO_3 captures a proton from $H^+(H_2O)_4$ along with a photo-generated electron, and forms 1H@WO_3. $[(H_2O)_4]_{HP}$ and $[(H_2O)_4]_{bulk}$ differentiate water cluster in the Helmholtz plane and bulk liquid. (b) Atomic structures of key intermediates in oxygen reduction reactions. 4H@WO_3 reacts

with O_2, forming $HO_2^{\bullet}$ or H_2O_2. δ± indicates a partial electron transfer between the molecule and the surface. Only the supported WO_3 monolayer is shown, and the TiO_2 substrate is hidden. (c) Potential energy diagram of oxygen reduction reactions.

Electronic structure and charge carrier localization for WO_3/a-TiO_2

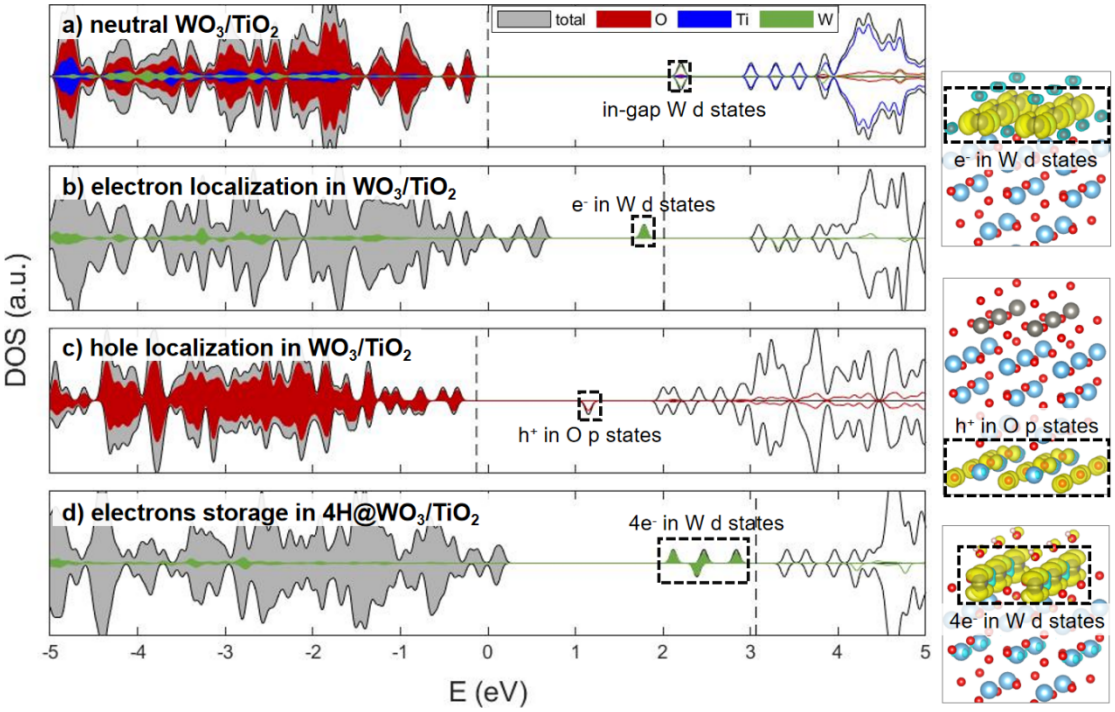

Figure 6. **Electronic structure analysis of the m-WO_3 monolayer supported on a-TiO_2(001).** Density of states (DOS) of **a)** Neutral WO_3/TiO_2. **b)** One photo-generated electron transferred from TiO_2 to WO_3 and localizes in W d states. **c)** One photo-generated hole localizes in O p states on the bottom a-TiO_2(001) surface. **d)** 4H@WO_3/TiO_2 with 4 protons adsorbed on WO_3 terminal oxygens and 4 electrons stored in W d states. The Fermi level of neutral WO_3/TiO_2 is set as zero. Dashed lines are Fermi levels of each system. Corresponding spin density configurations of localized charge carriers are shown on the right. Only PDOS of charge-carrier storage elements are shown.

The electron-hole pair separation and electron storage mechanism are further depicted by the analysis of the electronic structure, plotting the density of states. The WO_3/TiO_2 valence band mainly consists of O p states, the conduction band mainly consists of Ti d states, and W d orbitals introduce a gap state 0.8 eV below the conduction band (Figure 6a). Upon electron-hole pair generation, the photo-generated electrons tend to migrate to lower energy from the TiO_2 conduction band to the W gap states in the WO_3 monolayer (Figure 6b), where they can either participate in reduction reactions or be stored. Meanwhile, photo-generated holes tend to be trapped in surface O p states at the part of the TiO_2 substrate which is not covered by WO_3, modeled here by the bottom surface of the slab (Figure 6c), where they can participate in oxidation reactions. The charge carrier localization can be characterized by both the electron/hole induced gap states in the DOS and the spin density configurations on the right. This physical separation of electrons and holes hinders electron-hole recombination, which mitigates the charge-carrier recombination in TiO_2, thus increasing the photon absorption efficiency and the catalyst performance [9]. When WO_3/TiO_2 is fully charged, WO_3/TiO_2 is protonated to 4H@WO_3

(normalized to a p(2×2) supercell) and W d gap states become occupied with four electrons (Figure 6d). The net Bader charge of W in bare WO_3/TiO_2 is +2.79 e, but drops to +2.60 e in $4H@WO_3$, in line with a transition of W(VI) to W(V). Note that the change of Bader charge is fractional and does not correspond to a complete electron, as is usually the case. Such electron storage and W valence state transition has been observed by ESR measurements [18].

Conclusions

Using *ab initio* calculations, we explore the properties of m-WO_3(001) layers on a a-TiO_2(001) surface, including the epitaxy, surface structures in ambient conditions, and the electronic structure. We reveal the reversible charge storage mechanism of WO_3/TiO_2 at the surface.

The supported m-WO_3(001) monolayer is reconstructed and has 1 ML terminal oxygen coverage, doubled from the non-supported m-WO_3(001) surface (1/2 ML). Also, m-WO_3(001) favors monolayer thickness rather than stacking into multilayers on a-TiO_2(001), since WO_3 interlayer adhesion is weak. Plus, m-WO_3(001) multilayers on a-TiO_2(001) possess uncompensated polarity like many other metal-oxide ultrathin-layers.

Both exposed TiO_2 surface and supported WO_3 monolayer are sensitive to the environment. If the experiment is performed in an air-equilibrated gas-phase reactor, a common setup for photocatalytic reactions, the exposed a-TiO_2(001) surface will be hydrated into $2H_2O@TiO_2$, while the supported m-WO_3(001) monolayer remains bare. However, both TiO_2 surface and WO_3 monolayer may have interaction with H_2O/O_2 and transit into other surface phases, when experimental condition (H_2O/O_2 chemical potential) is changed. If the experiment is performed in the gas-phase reactor at raised temperature and reductive condition, a common setup for NO_x selective catalytic reduction reactions, TiO_2 surface will be in the $2H_2O@TiO_2$ phase, while WO_3 monolayer will be hydrogenated into $H@WO_3$. Also, both the TiO_2 surface and the WO_3 monolayer may have interaction with H_2O/H_2 and transit into other phases, when experimental condition (H_2O/H_2 chemical potential) is changed.

If the experiment is performed in acidic aqueous solvent, a common setup for WO_3/TiO_2 reversible charge storage, the WO_3 monolayer will be protonated at different levels (1-$4H@WO_3$) depending on the applied potential. With light radiation, bare WO_3 monolayer absorbs protons from the solvent along with photo-generated electrons from TiO_2, turning into $4H@WO_3$. When radiation is removed, $4H@WO_3$ releases the protons and stored electrons, turning back into bare WO_3 monolayer. The product of O_2 reduction with stored electrons may be either $HO_2^{\bullet}$ or H_2O_2, which can participate in reactions in the dark. This reversible proton-electron storage mechanism accounts for the experimental observation that WO_3/TiO_2 remains reactive minutes after the light radiation is removed.

Electronic structure analysis reveals that WO_3 also promotes photon absorption efficiency of TiO_2 by assisting electron-hole pair separation. W induced gap states trap the photo-generated electrons, while TiO_2 O states trap the holes. This mechanism accounts for the experimental observation that WO_3/TiO_2 has higher catalytic efficiency than pure TiO_2.

Acknowledgments

Funding: The work was supported by the U.S. Defense Threat Reduction Agency under Award Number HDTR1211001612. Computations in this work were performed on the Hoffman2 cluster

at UCLA Institute for Digital Research and Education (IDRE), and the Bridges2 cluster at Extreme Science and Engineering Discovery Environment (XSEDE) supported by National Science Foundation Grant No. ACI-1548562, through allocation TGCHE170060.

Competing interests: The authors declare no competing interests.

Author contributions: P.S. conceptualized and supervised the project. Y.L. performed the calculations with support from D.C., G.Y. and Z.W.. Y.L., D.C. and P.S. prepared the draft.

Supporting information: Free energy calculation methods and results, corresponding geometries, electronic structures, and DFT performance benchmark.

References

1. Schneider, J.; Matsuoka, M.; Takeuchi, M.; Zhang, J.; Horiuchi, Y.; Anpo, M.; Bahnemann, D. W., Understanding TiO2 photocatalysis: mechanisms and materials. *Chem Rev* **2014,** *114* (19), 9919-86.
2. De Angelis, F.; Di Valentin, C.; Fantacci, S.; Vittadini, A.; Selloni, A., Theoretical studies on anatase and less common TiO2 phases: bulk, surfaces, and nanomaterials. *Chem Rev* **2014,** *114* (19), 9708-53.
3. Meng, A.; Zhang, L.; Cheng, B.; Yu, J., Dual Cocatalysts in TiO(2) Photocatalysis. *Adv Mater* **2019,** *31* (30), e1807660.
4. Tae Kwon, Y.; Yong Song, K.; In Lee, W.; Jin Choi, G.; Rag Do, Y., Photocatalytic Behavior of WO3-Loaded TiO2 in an Oxidation Reaction. *Journal of Catalysis* **2000,** *191* (1), 192-199.
5. Chai, S. Y.; Kim, Y. J.; Lee, W. I., Photocatalytic WO3/TiO2 nanoparticles working under visible light. *Journal of Electroceramics* **2006,** *17* (2-4), 909-912.
6. Park, J.; Lim, J.; Park, Y.; Han, D. S.; Shon, H. K.; Hoffmann, M. R.; Park, H., In Situ-Generated Reactive Oxygen Species in Precharged Titania and Tungsten Trioxide Composite Catalyst Membrane Filters: Application to As(III) Oxidation in the Absence of Irradiation. *Environ Sci Technol* **2020,** *54* (15), 9601-9608.
7. Lin, C. F.; Wu, C. H.; Onn, Z. N., Degradation of 4-chlorophenol in TiO2, WO3, SnO2, TiO2/WO3 and TiO2/SnO2 systems. *J Hazard Mater* **2008,** *154* (1-3), 1033-9.
8. Guo, H.; Jiang, N.; Wang, H.; Lu, N.; Shang, K.; Li, J.; Wu, Y., Degradation of antibiotic chloramphenicol in water by pulsed discharge plasma combined with TiO(2)/WO(3) composites: mechanism and degradation pathway. *J Hazard Mater* **2019,** *371*, 666-676.
9. Tatsuma, T.; Saitoh, S.; Ohko, Y.; Fujishima, A., TiO2−WO3 Photoelectrochemical Anticorrosion System with an Energy Storage Ability. *Chemistry of Materials* **2001,** *13* (9), 2838-2842.
10. Tatsuma, T.; Saitoh, S.; Ngaotrakanwiwat, P.; Ohko, Y.; Fujishima, A., Energy Storage of TiO2−WO3 Photocatalysis Systems in the Gas Phase. *Langmuir* **2002,** *18* (21), 7777-7779.
11. Ngaotrakanwiwat, P.; Tatsuma, T.; Saitoh, S.; Ohko, Y.; Fujishima, A., Charge–discharge behavior of TiO2–WO3photocatalysis systems with energy storage ability. *Phys. Chem. Chem. Phys.* **2003,** *5* (15), 3234-3237.
12. Tatsuma, T.; Takeda, S.; Saitoh, S.; Ohko, Y.; Fujishima, A., Bactericidal effect of an energy storage TiO2–WO3 photocatalyst in dark. *Electrochemistry Communications* **2003,** *5* (9), 793-796.
13. Alemany, L. J.; Lietti, L.; Ferlazzo, N.; Forzatti, P.; Busca, G.; Giamello, E.; Bregani, F., Reactivity and Physicochemical Characterization of V2O5-WO3/TiO2 De-NO Catalysts. *Journal of Catalysis* **1995,** *155* (1), 117-130.
14. Busca, G.; Lietti, L.; Ramis, G.; Berti, F., Chemical and mechanistic aspects of the selective catalytic reduction of NO by ammonia over oxide catalysts: A review. *Applied Catalysis B: Environmental* **1998,** *18* (1-2), 1-36.
15. Lai, J.-K.; Wachs, I. E., A Perspective on the Selective Catalytic Reduction (SCR) of NO with NH3 by Supported V2O5–WO3/TiO2 Catalysts. *ACS Catalysis* **2018,** *8* (7), 6537-6551.
16. Tennakone, K.; Ileperuma, O. A.; Bandara, J. M. S.; Kiridena, W. C. B., TiO2and WO3semiconductor particles in contact: photochemical reduction of WO3to the non-stoichiometric blue form. *Semiconductor Science and Technology* **1992,** *7* (3), 423-424.
17. Sajjad, A. K. L.; Shamaila, S.; Tian, B.; Chen, F.; Zhang, J., One step activation of WOx/TiO2 nanocomposites with enhanced photocatalytic activity. *Applied Catalysis B: Environmental* **2009,** *91* (1-2), 397-405.

18. Zhao, D.; Chen, C.; Yu, C.; Ma, W.; Zhao, J., Photoinduced Electron Storage in WO3/TiO2 Nanohybrid Material in the Presence of Oxygen and Postirradiated Reduction of Heavy Metal Ions. *The Journal of Physical Chemistry C* **2009,** *113* (30), 13160-13165.

19. Khan, H.; Rigamonti, M. G.; Patience, G. S.; Boffito, D. C., Spray dried TiO2/WO3 heterostructure for photocatalytic applications with residual activity in the dark. *Applied Catalysis B: Environmental* **2018,** *226*, 311-323.

20. Zhou, G.; Zhao, T.; Qian, R.; Xia, X.; Dai, S.; Alsaedi, A.; Hayat, T.; Pan, J. H., Decorating (001) dominant anatase TiO2 nanoflakes array with uniform WO3 clusters for enhanced photoelectrochemical water decontamination. *Catalysis Today* **2019,** *335*, 365-371.

21. Suarez Negreira, A.; Wilcox, J., Role of WO3 in the Hg Oxidation across the V2O5–WO3–TiO2 SCR Catalyst: A DFT Study. *The Journal of Physical Chemistry C* **2013,** *117* (46), 24397-24406.

22. Kresse, G.; Hafner, J., Ab initio molecular dynamics for liquid metals. *Phys Rev B Condens Matter* **1993,** *47* (1), 558-561.

23. Kresse, G.; Furthmüller, J., Efficiency of ab-initio total energy calculations for metals and semiconductors using a plane-wave basis set. *Computational Materials Science* **1996,** *6* (1), 15-50.

24. Kresse, G.; Furthmuller, J., Efficient iterative schemes for ab initio total-energy calculations using a plane-wave basis set. *Phys Rev B Condens Matter* **1996,** *54* (16), 11169-11186.

25. Perdew, J. P.; Burke, K.; Ernzerhof, M., Generalized Gradient Approximation Made Simple. *Phys Rev Lett* **1996,** *77* (18), 3865-3868.

26. Kresse, G.; Joubert, D., From ultrasoft pseudopotentials to the projector augmented-wave method. *Physical Review B* **1999,** *59* (3), 1758-1775.

27. Steinmann, S. N.; Corminboeuf, C., A generalized-gradient approximation exchange hole model for dispersion coefficients. *J Chem Phys* **2011,** *134* (4), 044117.

28. Steinmann, S. N.; Corminboeuf, C., Comprehensive Benchmarking of a Density-Dependent Dispersion Correction. *J Chem Theory Comput* **2011,** *7* (11), 3567-3577.

29. Dudarev, S. L.; Botton, G. A.; Savrasov, S. Y.; Humphreys, C. J.; Sutton, A. P., Electron-energy-loss spectra and the structural stability of nickel oxide: An LSDA+U study. *Physical Review B* **1998,** *57* (3), 1505-1509.

30. Cococcioni, M.; de Gironcoli, S., Linear response approach to the calculation of the effective interaction parameters in theLDA+Umethod. *Physical Review B* **2005,** *71* (3).

31. Heyd, J.; Scuseria, G. E.; Ernzerhof, M., Hybrid functionals based on a screened Coulomb potential. *The Journal of Chemical Physics* **2003,** *118* (18), 8207-8215.

32. Liu, D.; Zi, W.; Sajjad, S. D.; Hsu, C.; Shen, Y.; Wei, M.; Liu, F., Reversible Electron Storage in an All-Vanadium Photoelectrochemical Storage Cell: Synergy between Vanadium Redox and Hybrid Photocatalyst. *ACS Catalysis* **2015,** *5* (4), 2632-2639.

33. Shifu, C.; Lei, C.; Shen, G.; Gengyu, C., The preparation of coupled WO3/TiO2 photocatalyst by ball milling. *Powder Technology* **2005,** *160* (3), 198-202.

34. Selloni, A., Crystal growth: Anatase shows its reactive side. *Nat Mater* **2008,** *7* (8), 613-5.

35. Gong, X. Q.; Selloni, A., Reactivity of anatase TiO(2) nanoparticles: the role of the minority (001) surface. *J Phys Chem B* **2005,** *109* (42), 19560-2.

36. Monkhorst, H. J.; Pack, J. D., Special points for Brillouin-zone integrations. *Physical Review B* **1976,** *13* (12), 5188-5192.

37. Vuurman, M. A.; Wachs, I. E.; Hirt, A. M., Structural determination of supported vanadium pentoxide-tungsten trioxide-titania catalysts by in situ Raman spectroscopy and x-ray photoelectron spectroscopy. *The Journal of Physical Chemistry* **1991,** *95* (24), 9928-9937.
38. Hilbrig, F.; Goebel, H. E.; Knoezinger, H.; Schmelz, H.; Lengeler, B., X-ray absorption spectroscopy study of the titania- and alumina-supported tungsten oxide system. *The Journal of Physical Chemistry* **1991,** *95* (18), 6973-6978.
39. Goniakowski, J.; Noguera, C.; Giordano, L., Prediction of uncompensated polarity in ultrathin films. *Phys Rev Lett* **2007,** *98* (20), 205701.
40. Liu, Z.; Lu, Y.; Yuan, L.; Ma, L.; Zheng, L.; Zhang, J.; Hu, T., Selective catalytic reduction of NOx with H2 over WO3 promoted Pt/TiO2 catalyst. *Applied Catalysis B: Environmental* **2016,** *188*, 189-197.
41. Nørskov, J. K.; Rossmeisl, J.; Logadottir, A.; Lindqvist, L.; Kitchin, J. R.; Bligaard, T.; Jónsson, H., Origin of the Overpotential for Oxygen Reduction at a Fuel-Cell Cathode. *The Journal of Physical Chemistry B* **2004,** *108* (46), 17886-17892.
42. Cheng, D.; Wei, Z.; Zhang, Z.; Broekmann, P.; Alexandrova, A. N.; Sautet, P., Restructuring and Activation of Cu(111) under Electrocatalytic Reduction Conditions. *Angew Chem Int Ed Engl* **2023**, e202218575.